Journal of Histochemistry & Cytochemistry 2015, Vol. 63(1) 8–21

DOI: 10.1369/0022155414559590
jhc.sagepub.com
SAGE

Study of the Development of the Mouse Thoracic Aorta Three-Dimensional Macromolecular Structure using Two-Photon Microscopy

Leah M. Zadrozny, Edward B. Neufeld, Bertrand M. Lucotte, Patricia S. Connelly, Zu-Xi Yu, Lam Dao, Li-Yueh Hsu, and Robert S. Balaban

Laboratory of Cardiac Energetics (LMZ, EBN, BML, LD, LYH, RSB); Electron Microscopy Core Facility (PSC); and Pathology Core (ZXY), NIH Heart, Lung and Blood Institute, National Institutes of Health, Bethesda, Maryland, USA

Summary

Using the intrinsic optical properties of collagen and elastin, two-photon microscopy was applied to evaluate the three-dimensional (3D) macromolecular structural development of the mouse thoracic aorta from birth to 60 days old. Baseline development was established in the Scavenger Receptor Class B Type I-Deficient, Hypomorphic Apolipoprotein ER61 (SR-BI KO/ApoeR61$^{h/h}$) mouse in preparation for modeling atherosclerosis. Precise dissection enabled direct observation of the artery wall in situ. En-face, optical sectioning of the aorta provided a novel assessment of the macromolecular structural development. During aortic development, the undulating lamellar elastin layers compressed consistent with the increases in mean aortic pressure with age. In parallel, a net increase in overall wall thickness ($p<0.05$, in day 60 compared with day 1 mice) occurred with age whereas the ratio of the tunicas adventitia and media to full aortic thickness remained nearly constant across age groups (~1:2.6, respectively). Histochemical analyses by brightfield microscopy and ultrastructure validated structural proteins and lipid deposition findings derived from two-photon microscopy. Development was associated with decreased decorin but not biglycan proteoglycan expression. This non-destructive 3D in situ approach revealed the aortic wall microstructure development. Coupling this approach with the intrinsic optical properties of the macromolecules may provide unique vascular wall 3D structure in many pathological conditions, including aortic atherosclerosis, dissections and aneurysms. (J Histochem Cytochem 63:8–21, 2015)

Keywords

collagen, elastin, two-photon microscopy, aorta, decorin, biglycan, atherosclerosis

Introduction

The development of the vascular anatomy at a subcellular level is important for understanding the relationship of genetic diseases affecting the macromolecular elements to the role of the macromolecules in common disease processes, such as atherosclerosis. Much of the information collected on the development of vascular macromolecular structures has involved traditional imaging modalities including histopathology and electron microscopy (EM). More recently, nonlinear optical microscopy (NLOM) has been utilized. NLOM describes a group of imaging modalities that are sensitive to specific molecules and structures in biological systems, which, when coupled together, can

Received for publication May 22, 2014; accepted September 30, 2014.

Corresponding Author:
Leah M. Zadrozny, DVM, Molecular Pathology Fellow, Laboratory of Cardiac Energetics, National Heart, Lung, and Blood Institute, National Institutes of Health, 10 Center Drive, Building 10, B1D219, Bethesda, MD 20892-1424, USA.
E-mail: zadroznylm@nhlbi.nih.gov

provide important information regarding conditions such as cardiovascular disease as well as cancer development, lipid metabolism, embryogenesis and skin biology (Zipfel et al. 2003; Supatto et al. 2005; Yue et al. 2011). Examples include two-photon excitation fluorescence (TPEF), second-harmonic generation (SHG) and Coherent anti-Stokes Raman scattering (CARS). Multiphoton excitation in biological tissues typically relies on near infra-red light to excite the chromophores and provides inherent 3D spatial resolution with focused excitation. Because linear absorption and scattering in tissues at these wavelengths are generally smaller than those at visible wavelengths, greater imaging depth can be achieved with multiphoton excitation than with linear confocal microscopy (Yue et al. 2011). The penetration depth and 3D resolution capabilities in multiphoton excitation bypass the need for physical sectioning and subsequent data registration required in histopatholothy and other imaging modalities.

Recently, TPEF has emerged as a powerful method for label-free imaging of living tissues and cells as well as fresh and formalin-fixed postmortem samples. TPEF was first demonstrated in 1990 (Denk et al. 1990), and provides reduced photodamage and fluorophore photobleaching. In TPEF, the target molecules absorb two excitation photons emitted from a pulsed laser to achieve an electron-excited state, which then emit a single fluorescence photon of greater energy than the incident photons (de Grauw et al. 1999). TPEF microscopy has been applied to biological imaging by utilizing intrinsic fluorescence or extrinsic labeling of molecular structures within numerous systems including musculoskeletal, urinary as well as neurological and cardiovascular. With regard to vascular imaging, elastin fibers are readily visualized due the presence of endogenous chromophores found, for example, within certain amino acid chains rich in tryptophan and tyrosine, which imparts inherent autofluorescence (Richards-Kortum and Sevick-Muraca 1996). Low-density lipoprotein (LDL) binding, proteoglycan (PG) labeling, and subendothelial lipid deposition can also be effectively imaged using TPEF in combination with the appropriate fluorophores and fluorescent lipid dyes, including Nile Red (NR) (Yu et al. 2007; Kwon et al. 2008). It is important to note though, as previously described by Kwon et al. (2008), that the fluorescence emission spectra of elastin is quite broad and shifts with varying excitation frequency, suggesting that elastin has multiple chromophores contributing to fluorescence emission (Kwon et al. 2008). This must be taken into consideration when choosing fluorescent probes to minimize any potential overlap in emission spectra.

SHG, another example of NLOM, is a nonlinear scattering process allowing for the visualization of unstained, endogenous noncentrosymmetric proteins such as fibrillar collagen (Strupler et al. 2007). Similar to TPEF, SHG provides intrinsic three-dimensionality as well as increased tissue penetration depth.

The present study offers a new methodology combining previously described multiphoton microscopy with a novel, in situ dissection of the ventral (anterior) surface of the mouse thoracic aorta (VTA). This approach was used to complete a longitudinal analysis of the developing thoracic aorta in mice aged 1–60 days old (do). Additional benefits of this preparation included not having to: 1) mount blood vessels into a perfusion chamber, as required for some vascular experiments; 2) mount small vascular segments onto glass slides that are cover slipped and sealed for further multiphoton imaging, and; 3) perturb the vascular bed during in situ dissection. Although transmural physiological pressure is minimal in this preparation, the longitudinal stretch maintained mimics that in vivo, and compares to that obtained while mounted within a perfusion chamber. Longitudinal stretch is also not completely lost, as is the case when smaller vessel segments are dissected and mounted between a glass slide and cover slip. As a comparison, histopathology and EM were completed in parallel.

Although any strain of mouse could have been used for this preparation, we reasoned that a more useful control would be a strain that could be induced to form atherosclerosis. We chose the recently described SR-BI KO/ApoeR61$^{h/h}$ mouse model of atherosclerosis (Zhang et al. 2005), maintained under normal dietary conditions thereby limiting the induction of vasculopathy as a control condition. This was done so that future studies evaluating the macromolecular events associated with atherosclerosis in this model could be compared directly to these data using the approach documented herein.

Materials & Methods

Animals

SR-BI KO/ApoER61$^{h/h}$ mice obtained from Dr. Alan Remaley at the National Heart Lung and Blood Institute (NHLBI) in Bethesda, MD, were bred, as previously described (Zhang et al. 2005). Gestating and neonatal mice (<3 weeks old) were fed a breeder diet (20% protein, 9% fat, 5% fiber, LabDiet, mouse breeder diet 5021) and weanling mice (>3 weeks old) were fed a normal chow (NC) diet (18% protein, 4% fat, 5% fiber, Zeigler Feed, NIH-31 open formula). All experiments on animals were performed according to the research protocol (H-0257) approved by the Animal Care and Use Committee of the NHLBI at the National Institutes of Health.

Mouse Thoracic Aorta Preparation for Multiphoton Microscopy

VTAs were dissected within male and female mice fed breeder chow aged 1, 10 and 20do, and NC aged 30 and 60do (n=5 per age group). Mice ≤20do were euthanized

with a lethal dose of sodium pentobarbital (150 mg/kg) injected intraperitoneally and otherwise prepared for dissection according to our approved animal study. Mice >20do were placed in an anesthesia box for induction and then ventilated by a nose cone with a mixture of 2.5% isoflurane in oxygen and euthanized via a double thoracotomy. The caudal vena cava was transected and blood was removed from the heart and thoracic aorta by perfusion of the left ventricle with <6 ml cold, 1× phosphate-buffer solution (PBS) followed by slow perfusion with NR (100 μg/ml in 200 μL sterile saline, Life Technologies; Invitrogen; Grand Island, NY) for lipid staining. While secured on an ice cold aluminum block, mice were prepared to expose the heart, bilateral kidneys and the entire length of the thoracic aorta intact by sharp dissection. The abdominal organs were removed and the mesenteric vessels were transected at the level of the abdominal aorta. VTAs were prepared by removing the perivascular adipose tissue. Intercostal arteriolar branches were left intact. The entire length of the thoracic aorta, while still attached to the heart, kidneys and vertebral column, remained patent. The limbs were disarticulated and removed along with the skin and tail, and the ribs and soft tissue were trimmed bilaterally to within 5 mm of the vertebral column (Fig. 1). These preparations were pinned in place with insect specimen mounting pins (Fine Science Tools; Foster City, CA), on either side of the vertebral column onto 20% agar gel platforms. Additional pins were appropriately placed between the 3rd and 5th-, the 8th and 9th-, and the 11th and 12th intercostal branches to consistently position the proximal, mid- and distal VTAs across all aortic preparations for imaging upon completion of a thorough scan of the entire VTA. Imaging of the dorsal (posterior) surface of the thoracic aorta, with intact intercostal ostia, was beyond the depth penetration capability of the Leica SP5 laser (MaiTai HP, Spectra-Physics/Newport; Mountain View, CA). Prior to imaging, aortas were submerged in optical coupling gel (NHLBI-NIH), with a refractive index similar to that of water, or saline. Mid- and distal VTA images along with movies of the proximal VTA may be found in Fig. 2 and the Supplemental Materials section, respectively.

Multiphoton Laser Scanning Microscopy

In situ, two-photon images of the VTA were acquired from the luminal surface out to the aortic tunica adventitia. A Ti:sapphire laser (MaiTai DS, Spectra-Physics/Newport) was tuned to 820 nm for excitation. For the majority of the experiments, a water dipping 25×, 1.1 NA objective lens (Nikon; Tokyo, Japan) was used for both saline submerged and optical gel-coupled aortic preparations. Three photomultiplier tubes (PMTs) were used to collect the emitted photons in non-descanned mode and provided three spectral channels to separate collagen, elastin and the lipophyilic, exogenous probe, NR, as previously described (Kwon et al. 2008). Briefly, collagen SHG was detected at 395–410 nm (PMT I), elastin fluorescence at 435–495 nm (PMT II), and NR (lipid) fluorescence at 570–640 nm (PMT IV). Three-dimensional images from each PMT at 512×512 pixels, with a frame rate of 700 Hz, a 1.7 optical zoom and a step section of 1 μm were collected as a stack of images beginning at the luminal surface and ending at the tunica adventitia. Images were analyzed using ImageJ (NIH; Bethesda, MD) and applying independent component analysis (ICA) for signal to noise enhancement (Dao et al. 2014). Aortic wall thickness measurements were taken on the ventral (anterior) surface from the two-photon images at three standard positions: 3-, 6- and 9-o'clock. To determine the relationship between residual strain and IEL undulation, the distance between undulating peaks, or spatial frequency, was measured (n=15 measurements/mouse).

Independent Component Analysis

Our laboratory recently demonstrated the use of ICA (Dao et al. 2014) as a method to improve the signal-to-noise ratio but also the spatial discrimination in multi-probe fluorescence imaging experiments. In this application, we used ICA to primarily improve the spatial discrimination between the collagen, elastin and NR (lipid) signals. ICA requires that there be no spatial overlap between signals; i.e., only one signal originates from each pixel. In a preliminary study, we established that the spatial overlap between collagen SHG, elastin and NR fluorescence is minimal due to the high spatial resolution. Using this assumption, ICA permitted the determination of the best statistical solution of the images where the signal overlap between all three signals was minimized. This essentially removed the "cross-talk" between spectral channels. This is significant because the cross-talk from elastin to the other channels cannot be completely suppressed with conventional filters alone due to its broad emission spectrum (Kwon et al. 2008).

After the ICA analysis, a background threshold was determined to be the mean of the NR signal plus the standard deviation of this signal to improve the overall image contrast. The NR signal was used as a reference for the background, as it was the weakest signal collected. With the NR signal thresholded to zero, we used a background region of the image and created the threshold at the mean of the background signal plus the standard deviation of the background signal.

Given that this is a relatively new approach, we have provided raw data without ICA processing (Supplemental Fig. 1) along with the ICA processed data (Fig. 3) for comparison. We did not observe any image distortions or inappropriate signal distributions generated by the ICA image processing approach.

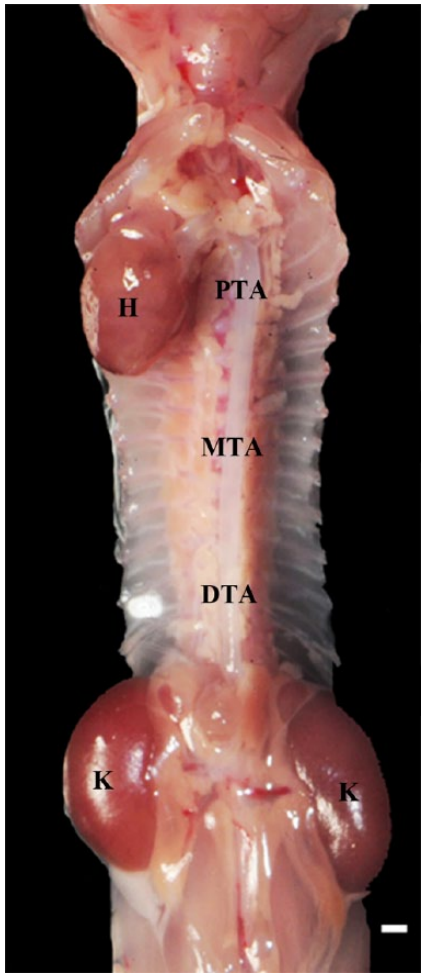

Figure 1. In situ dissection of the mouse thoracic aorta in dorsal recumbency. The heart (H), kidneys (K), and three regions of interest—the proximal (PTA), mid (MTA) and distal (DTA) thoracic aorta—are labeled. Multiphoton images are all depicted with the head and tail ends of the mice at the top and bottom of each image, respectively. Full-thickness z-stacks were obtained from the luminal to the adventitial surfaces of the ventral thoracic aorta. Scale, 1 mm.

Histopathology

An additional group of age-matched mice (n=5 per age group) was processed for histopathology and transmission EM. Thoracic aortas were perfusion-fixed with 4% paraformaldehyde, and transected at the levels of the aortic root, mid- and distal thoracic regions. Proximal to mid-thoracic segments were placed into 10% buffered formalin and embedded in paraffin. Serial cross sections were cut at the level of the proximal descending thoracic aorta and stained with hematoxylin and eosin (H&E), Movat's pentachrome ((collagen, elastin and glycosaminoglycans) Polysciences, Inc.; Warrington, PA), and Picrosirius Red ((collagen) Polysciences, Inc.) for morphological evaluations. Immunohistochemistry (IHC) was performed with an indirect peroxidase method. Paraffin sections were de-waxed, rehydrated and pretreated with Chondroitinase-ABC, (Seikagaku Biobusiness, 1U/ml) for 30 min at 37C. Primary antibodies against Decorin (1:200, R&D Systems; Minneapolis, MN) and Biglycan (1:75, Abcam; Cambridge, MA) were incubated overnight at 4C. Following PBS washing, sections were incubated with biotinylated secondary antibodies (ABC Elite kits, Vector Laboratories; Burlingame, CA), then with peroxidase-conjugated ABC reagent, according to the manufacturer's directions. The reactions were visualized using 3, 3'-diaminobenzidine (DAB) substrate (Vector Laboratories) for 5 min. Nuclei were then counterstained with hematoxylin. Negative controls were performed each time with omitted primary antibodies and all gave negative results. Histology images were taken using a Leica NB 4000 digital camera. Mid- to distal thoracic aortic segments were processed for EM as described below.

Electron Microscopy

Distal thoracic aortas were fixed with 2.5% glutaraldehyde, 4% paraformaldehyde, 0.12 M sodium cacodylate, post-fixed in 1% osmium tetroxide, block-stained in 1% uranyl acetate, dehydrated in graded ethanol solutions, and embedded inEMbed-812 (Electron Microscopy Sciences; Hatfield PA). Ultra-thin sections from the distal aortas were stained with uranyl acetate and lead citrate then examined on a JEM 1400 electron microscope (JEOL USA; Peabody MA) equipped with an AMT XR-111 digital camera (Advanced Microscopy Techniques Corporation; Woburn, MA). Semi-thin sections (0.5 μm) were taken from the blocks prepared for EM and stained with toluidine blue for lipid identification by light microscopy.

Statistical Analysis

All data are presented as mean ± SEM. Proximal VTA wall thickness, including the tunicas media and adventitia, was assessed and compared between age groups by two-tailed Student's t-test. The significance level was set at $p<0.05$.

Results

Multiphoton Analysis of the Proximal Thoracic Aorta

The 3D structural development of collagen and elastin was evaluated along the entire length of the VTA across all age groups, and z-stacks were obtained for post-image

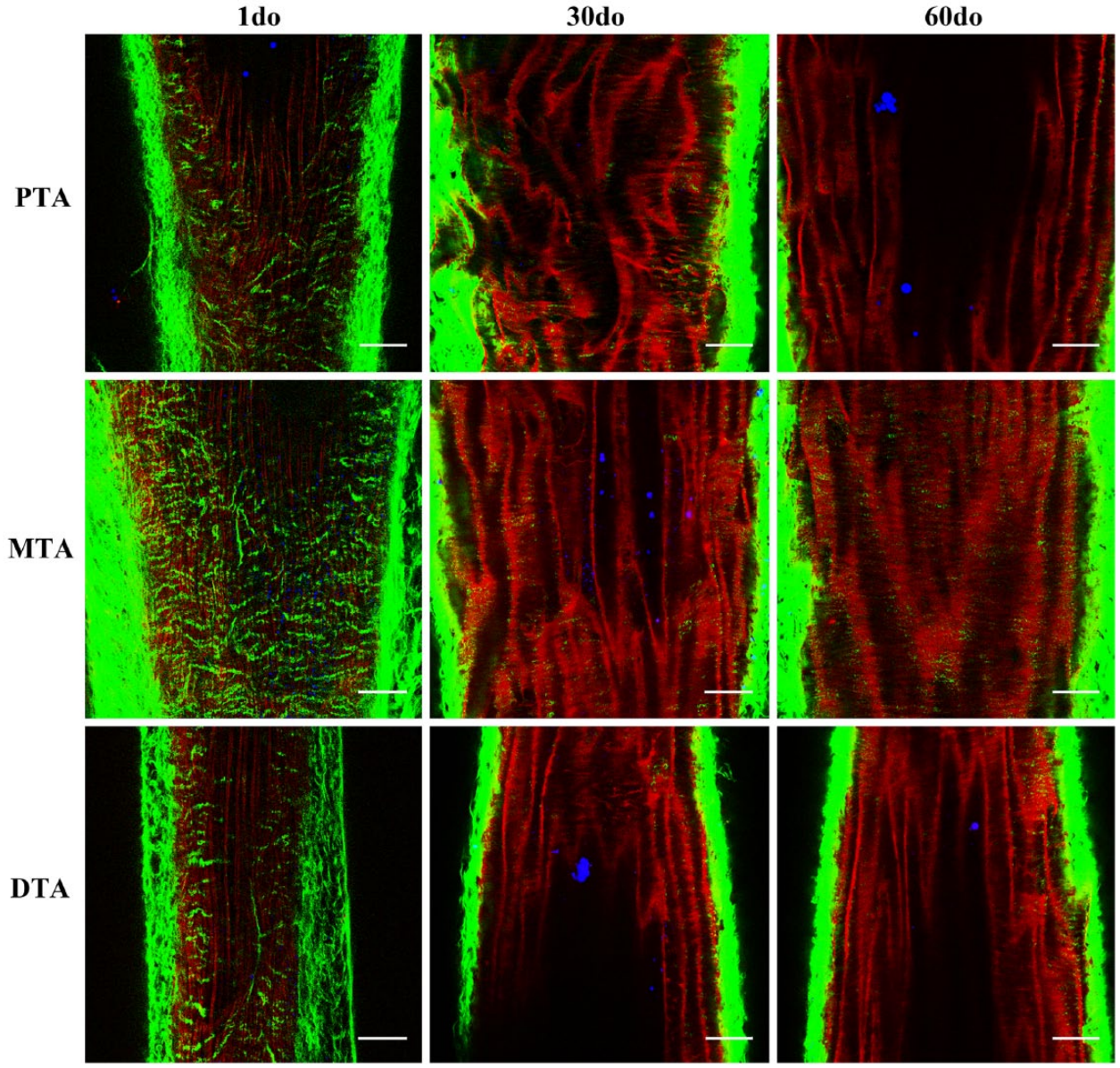

Figure 2. Multiphoton images from the proximal, mid and distal thoracic aorta (PTA, MTA and DTA) of 1 day old (do), 30do and 60do SR-BI$^{-/-}$/ApoeR61$^{h/h}$ mice. Images depict 1-µm-thick optical slices captured from full-thickness z-stacks within the tunica media. Sections are representative of the thoracic aortic regions of interest, as shown in the in situ mouse preparation in Figure 1, with the head and tail ends of the mice at the top and bottom of each image, respectively. Collagen (green), elastin (red) and lipid (blue) signals are merged after post-image processing by Independent Component Analysis (ICA). Scale, 50 µm.

processing from the proximal, mid- and distal VTA. Given the similarities observed within the vascular bed (Fig. 2), coupled with the fact that a predominance of atherosclerotic lesions occur at this site and within the aortic arch (Tangirala et al. 1995; McGillicuddy et al. 2001; Haidari et al. 2010) in mouse models induced to develop atherosclerosis, sections from the proximal VTA remained the primary focus.

The collagen and elastin microstructure formed a variably confluent, wavy meshwork of elastin throughout the tunica intima and tunica media around which variably dense, fibrillar strands of collagen were circumferentially arranged (best appreciated in cross sections; Fig. 3, Fig3video1.avi, Fig4video2.avi, Figure 4, and Supplemental movies I-X). The density of this matrix and overall abundance of elastin and collagen was interpreted to increase with age; however, the changes noted from 20–60 do mice were minimal. These findings are consistent with previous gene expression analyses, in which the expression of genes

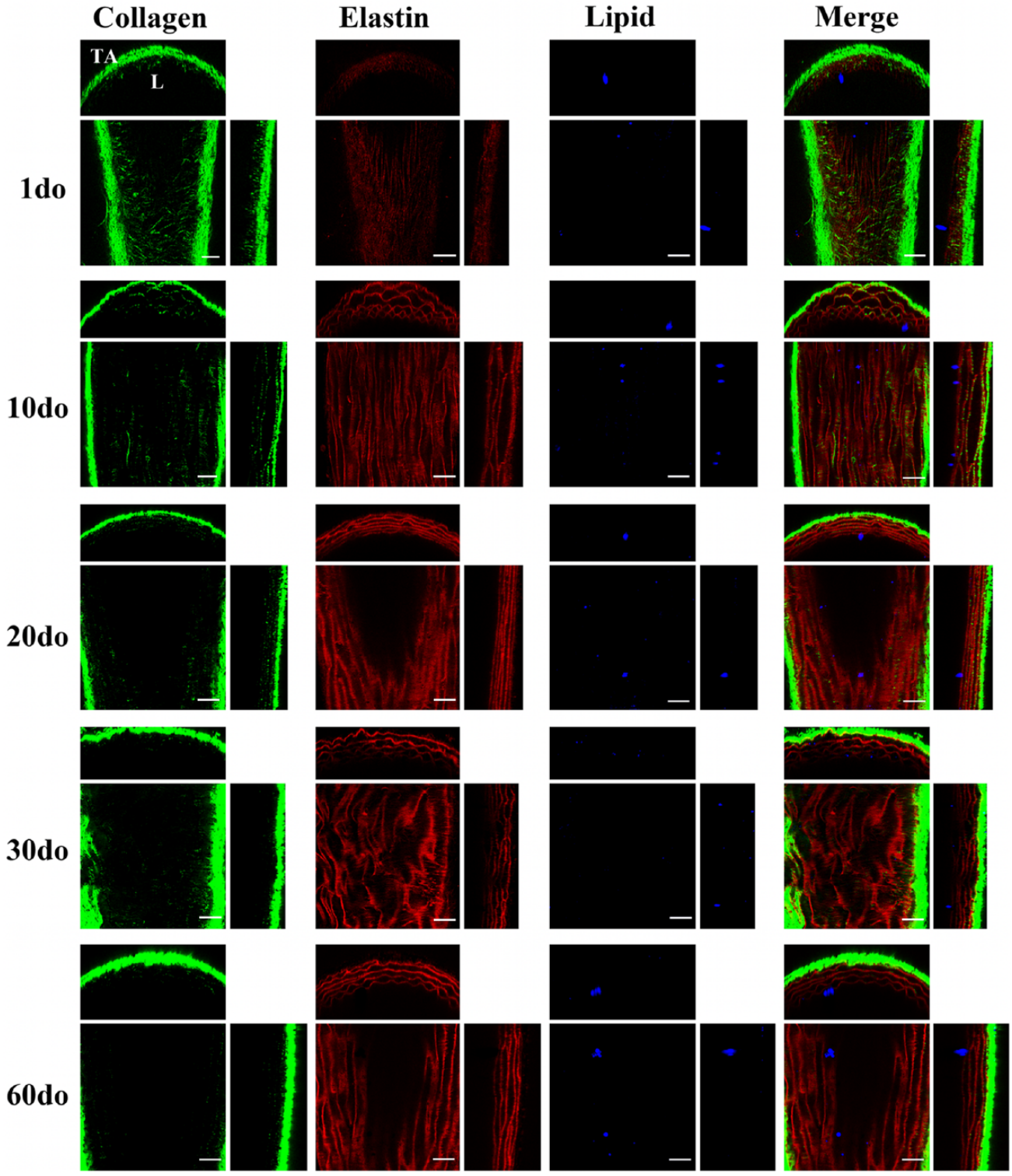

Figure 3. Multiphoton, in situ images acquired from the proximal ventral (anterior) thoracic aortas (VTAs) of representative SR-BI$^{-/-}$/ApoeR61$^{h/h}$ mice aged 1–60 days old (do). Images depict 1-µm-thick optical slices captured from full-thickness z-stacks within the tunica media of the proximal VTA. For each individual orthogonal panel, the center, top and right sections depict en-face (xy), cross/transverse (xz) and sagittal (yz) sections, respectively. Collagen second harmonic generation (SHG) is green, elastin auto-fluorescence is red and Nile Red (NR) lipid droplet fluorescence is blue. Independent component analysis (ICA) was applied to all z-stacks for post-image processing to eliminate signal overlap and background noise. For raw images, and full thickness movies, please refer to the Supplemental Materials section. L, lumen; TA, tunica adventitia. Scale, 50 µm.

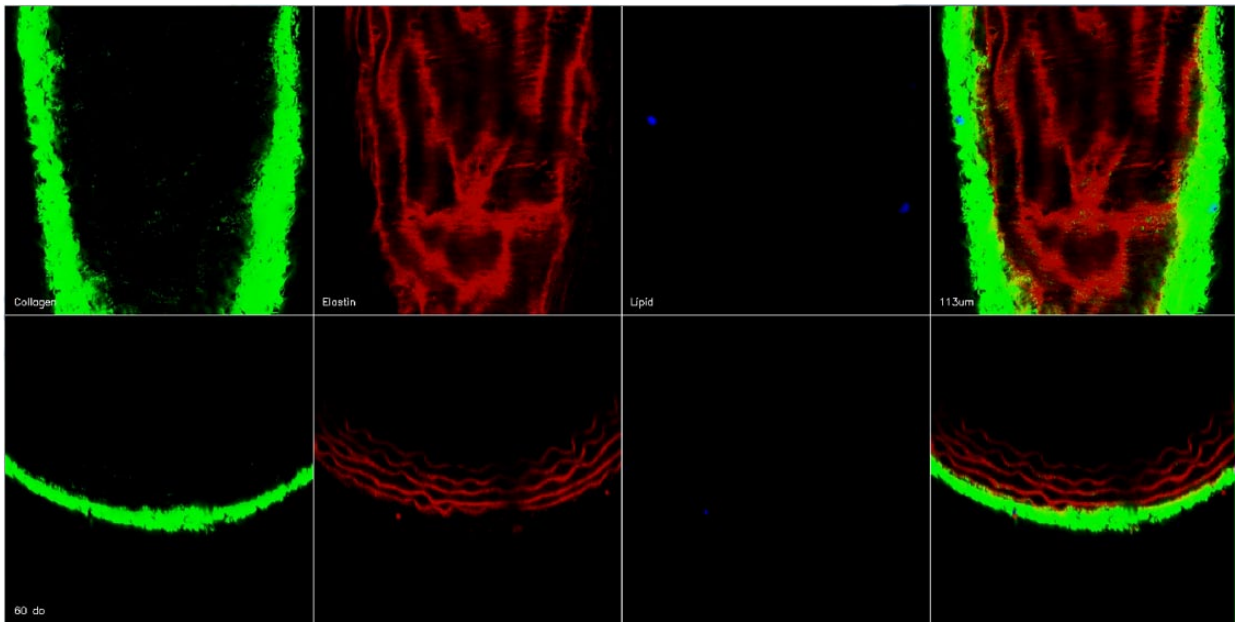

Fig3 video1. AVI video clips were produced from a full-thickness z-stack (ranging from ~150–200-μm-thick tissue image acquisitions) obtained within the ventral (anterior) surface of the proximal thoracic aorta of a representative SR-BI$^{-/-}$/ApoeR61$^{h/h}$ mouse aged 60 days old (do). En-face projections coupled with cross sections are provided. Collagen second harmonic generation (SHG) is green, elastin auto-fluorescence is red and Nile Red (NR) lipid droplet fluorescence is blue. Image acquisition was optimized during all experiments to fill the digitizer. ICA was applied during post-image processing and the elastin fluorescence signal was optimized across all age groups for comparison purposes. Additional movies are provided in the Supplemental Materials.

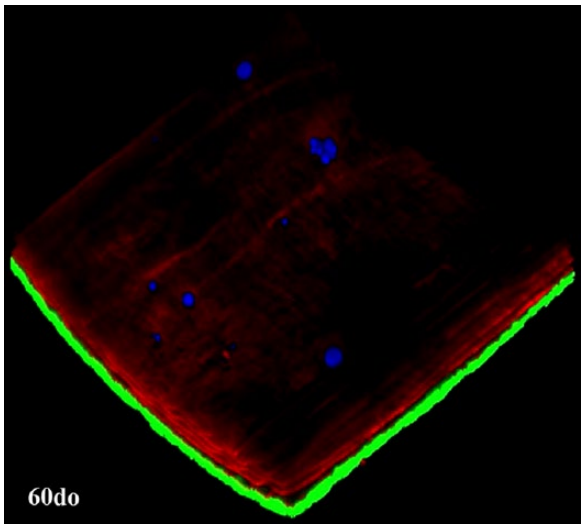

Fig4 video2. An AVI video clip produced from a maximum projection, three-dimensional (3D) rendering from a z-stack of the proximal ventral (anterior) thoracic aorta (VTA) of a representative SR-BI$^{-/-}$/ApoeR61$^{h/h}$ mouse aged 60 days old (do) is provided. For color scheme and post-image processing information, see Fig3video1. Additional 3D renderings are provided in the Supplemental Materials.

encoding proteins for collagen and elastin peaked at approximately 15 days postnatally, followed be a gradual decrease in expression 2–3 months thereafter (Kelleher et al. 2004; Wagenseil et al. 2009). Additionally, a markedly enhanced SHG signal was recorded when transitioning from the tunica media into the tunica adventitia where the collagen fibrils are more abundant and irregularly arranged, and this increased with age.

Lipid droplets were individualized or arranged as small clusters, ranging from 1–30 μm in diameter (Figs. 3–4, and Supplemental Movies I-X), and were visualized along the entirety of the VTA, primarily on the luminal surface within the vascular endothelium or directly beneath the internal elastic lamina (IEL). In previous experiments in our laboratory, di-8-ANEPPS (Invitrogen), a fluorescent probe that binds the vascular endothelium and phospholipid bilayer membranes, was administered through an intra-cardiac injection, as described for NR in the Materials & Methods. To help confirm lipid droplet location in the present study, en-face and cross-sectional movies have been included in the Supplemental Materials (Supplemental AVI movies XIII-XIV). Lipid droplets (black hollow spheres outlined in blue) are appreciated resting on the stained vascular endothelium (blue), indicating that the lipid droplets within this z-stack are likely captured on the vascular luminal surface directly on the endothelium and within the endothelial cell cytoplasm.

The average thoracic aortic wall thickness is summarized in Table 1. As expected, the average full thickness (FT) significantly increased with age ($p<0.05$) for mice

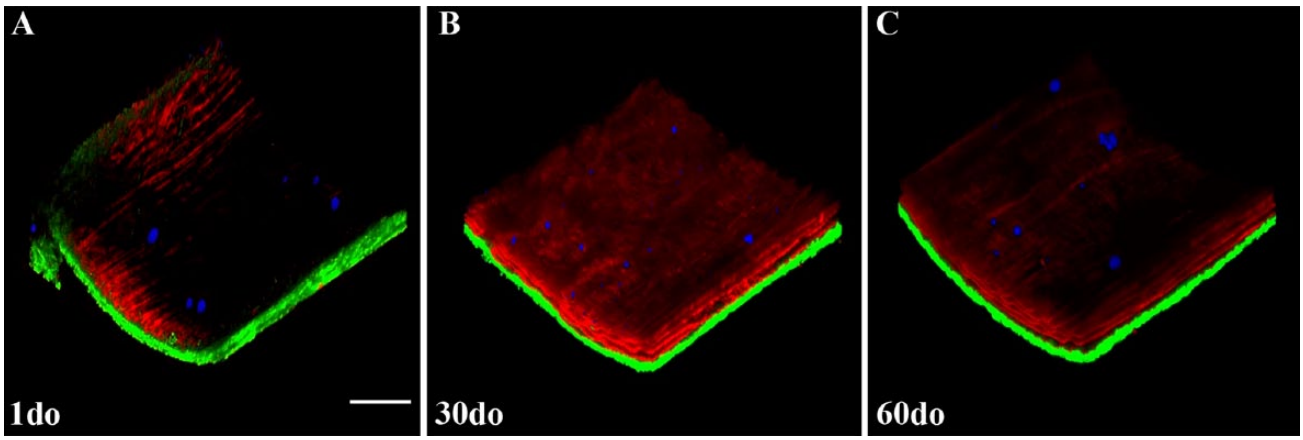

Figure 4. Three-dimensional, multiphoton, maximum projection renderings (approximate size 512×512×150-200 μm) from z-stacks of the proximal ventral (anterior) thoracic aortas (VTAs) of SR-BI$^{-/-}$/ApoeR61$^{h/h}$ mice aged 1, 30 and 60 days old (do). Collagen second harmonic generation (SHG) is green, elastin auto-fluorescence is red and Nile Red (NR) lipid droplet fluorescence is blue. Independent component analysis (ICA) was applied to all z-stacks for post-image processing. For a more detailed view, please refer to the movies in the Supplemental Materials. Scale bar, 50 μm.

Table 1. Average Proximal Thoracic Aortic Wall Thickness in SR-BI KO/ApoeR61$^{h/h}$ Transgenic Mice Fed Normal Chow.

Ventral (Anterior) Proximal Thoracic Aorta	1do	10do	20do	30do	60do
Full thickness (μm)	50.73 ± 2.66	58.71 ± 1.31	58.52 ± 2.10	67.51 ± 1.76	72.67 ± 2.80
Tunica adventitia thickness (μm)	15.74 ± 0.57	14.49 ± 0.44	16.57 ± 0.39	18.76 ± 0.32	21.96 ± 0.74
Tunica media thickness (μm)	34.99 ± 2.87	44.22 ± 0.88	41.95 ± 2.23	48.78 ± 1.72	50.71 ± 2.70
AT/FT (%)	31	24	28	28	30
MT/FT (%)	69	76	72	72	70

Values are mean ± SEM. Three to 5 animals per group with 3 wall thickness measurements per animal. AT, adventitial thickness; MT, medial thickness; FT, full thickness; do, days old.

aged 20do, 30do and 60do when compared with 1do mice (Fig. 5A). The ratios of the wall thickness of the tunicas adventitia and media to full aortic thickness exhibited the greatest significance when comparing 1do mice with 10do mice (p=0.032), whereas minimal significance was noted when comparing 1do mice with 30do mice (p=0.048) and 10do mice with 20do mice (p=0.047) (Fig. 5B). This indicates that, although the average VTA FT significantly increased with age, the individual layers increased proportionally in comparison to FT across the age groups.

The average distance between undulating peaks in the IEL is summarized in Table 2. The distance between peaks linearly increased from 10.61 ± 0.35 μm in 1do mice to 29.51 ± 0.90 μm in 20do mice and then began to plateau at 31.03 ± 0.35 μm and 32.27 ± 0.46 μm in 30 and 60do mice, respectively.

Histopathology Study

Histologically, proximal VTAs varied the most from 1do up to 20do (Fig. 6). The IEL, medial elastic laminae (MEL) and external elastic lamina (EEL) in 1do and 10do mice were undulated (Movat's pentachrome) and lined by plump endothelial cells (H&E). Lamellae began to flatten out and endothelial cells became more attenuated by 10do. Sections of the thoracic aorta fixed in Optical Cutting Temperature medium (Tissue-Tek® OCT, Miles; Elkhart, IN) frozen on dry ice and submitted to the NHLBI pathology core laboratory for lipid analysis using Oil-Red-O failed revealed lipid accumulation throughout all age groups (Oil-Red-O histology not shown).

Collagen deposition determined by picrosirius red stain showed the fibrillar structure of medial and adventitial collagen deposition with increased signal and accumulation in the adventitia of older mice (Fig. 6B, 6E, 6H, 6K and 6N). Movat's pentachrome collagen staining was most apparent within the tunica adventitia and muted throughout the interlamellar smooth muscle layers (Fig. 6C, 6F, 6I, 6L and 6O). These findings further support both the increased sensitivity and variation in collagen SHG signal observed with two-photon microscopy in the vessel wall. Movat's pentachrome stain revealed little proteoglycan deposition (green/blue)

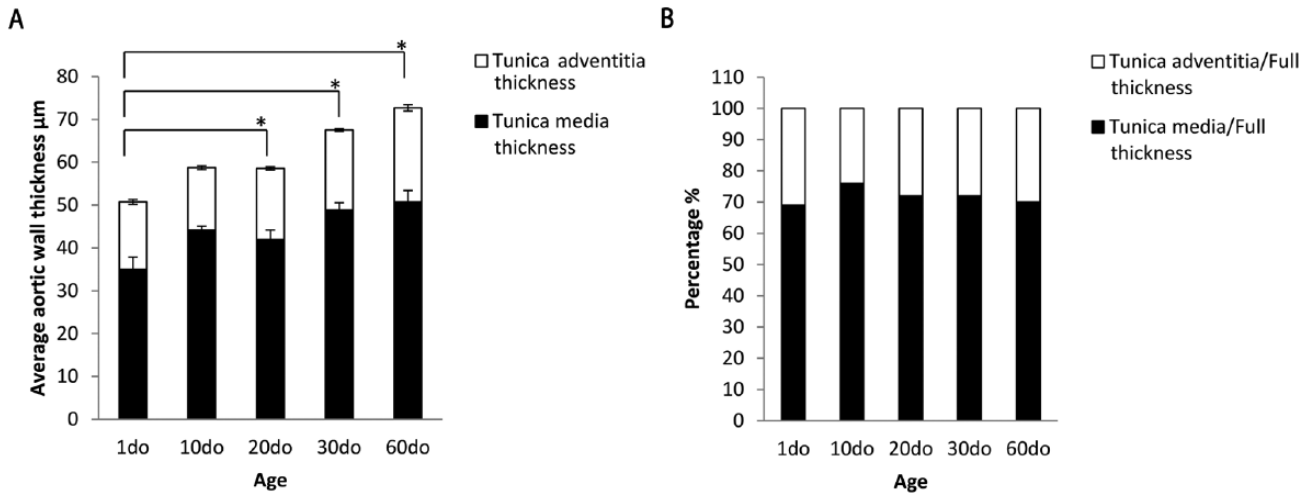

Figure 5. Bar graphs showing the average thoracic aortic wall thickness. (A) Average ventral (anterior) thoracic aortic (VTA) full thickness (FT) (total bar height) significantly increased with age (*p<0.05 for mice aged 20 days old (do), 30do and 60do when compared to 1do mice) with no significant change in 10do mice as compared with 20do mice. Values are mean ± SEM. (B) Ratios of the wall thickness of the tunica adventitia and tunica media to full VTA thickness. The greatest significance is exhibited when 1do mice are compared to 10do mice (p=0.032), and minimal significance when 1do mice are compared to 30do mice (p=0.048) and 10do mice are compared to 20do mice (p=0.047). This indicates that the thickness of the individual tunics within the thoracic aorta increases proportionally with age.

Table 2. Average Distance between Undulating Peaks in the Internal Elastic Lamina (IEL) in SR-BI KO/ApoeR61$^{h/h}$ Transgenic Mice Fed Normal Chow.

Ventral (Anterior) Proximal Thoracic Aorta	1do	10do	20do	30do	60do
Average distance between IEL peaks (µm)	10.61 ± 0.35	22.93 ± 0.46	29.51 ± 0.90	31.03 ± 0.35	32.27 ± 0.46

Values are mean ± SEM. Four to five animals per group with 15 internal elastic lamina (IEL) measurements per animal.

transmurally through the proximal thoracic aorta (Fig. 6C, 6F, 6I, 6L and 6O).

Immunoreactivity for decorin and biglycan, small leucine-rich repeat (SLRP) dermatan sulfate proteoglycans, yielded similar findings regarding subendothelial and adventitial deposition (Supplemental Fig. 2). The strongest immunoreactivity occurred in both the tunica adventitial collagen and subendothelium, while weaker positive reactivity occurred within the interlamellar layers of the media throughout all age groups. However, immunoreactivity of decorin within the tunica media appeared to decrease with age while remaining similar across age groups for biglycan. Intercostal ostia that were captured in cross sections exhibited strong positive immunoreactivity within the subendothelium and tunica media for both proteoglycans (Supplemental Fig. 2C and 2G–J).

Electron Microscopy Study

Sections from the distal thoracic aorta were evaluated. Distinct, circumferential layers of vascular smooth muscle cells were well defined at 1do and interposed between incompletely developed elastic laminae that exhibited occasional gaps along the length of individual lamina (Fig. 7). By 10do, five, nearly continuous elastic laminae were consistently discerned throughout the entirety of the thoracic aorta (images not shown). Variably sized, intracellular lipid droplets (up to 2 µm in diameter) were observed within endothelial cells (Fig. 7C, 7E, 7G–7I) and within smooth muscle cells (Fig. 7B, 7C, 7H–7I) directly beneath the IEL across all age groups. Lipid droplets were also present within the subendothelium of an intercostal ostial ridge of a 30do mouse captured in Figure 7F. Endothelial cell phagocytosis of lipid can be appreciated in multiple sections of all age groups (Fig. 7A). A focally extensive accumulation of variably sized, intimal lipid droplets admixed with calcified and mineralized debris was indicative of early atherosclerotic lesion formation in a 60do mouse (Fig. 7J). This was not considered a surprising finding though as morbidity did occasionally occur within our mouse colony due to cardiovascular disease in aged (less than 1yo) SR-BI KO/ApoeR61$^{h/h}$ mice fed the NC diet. Despite finding evidence

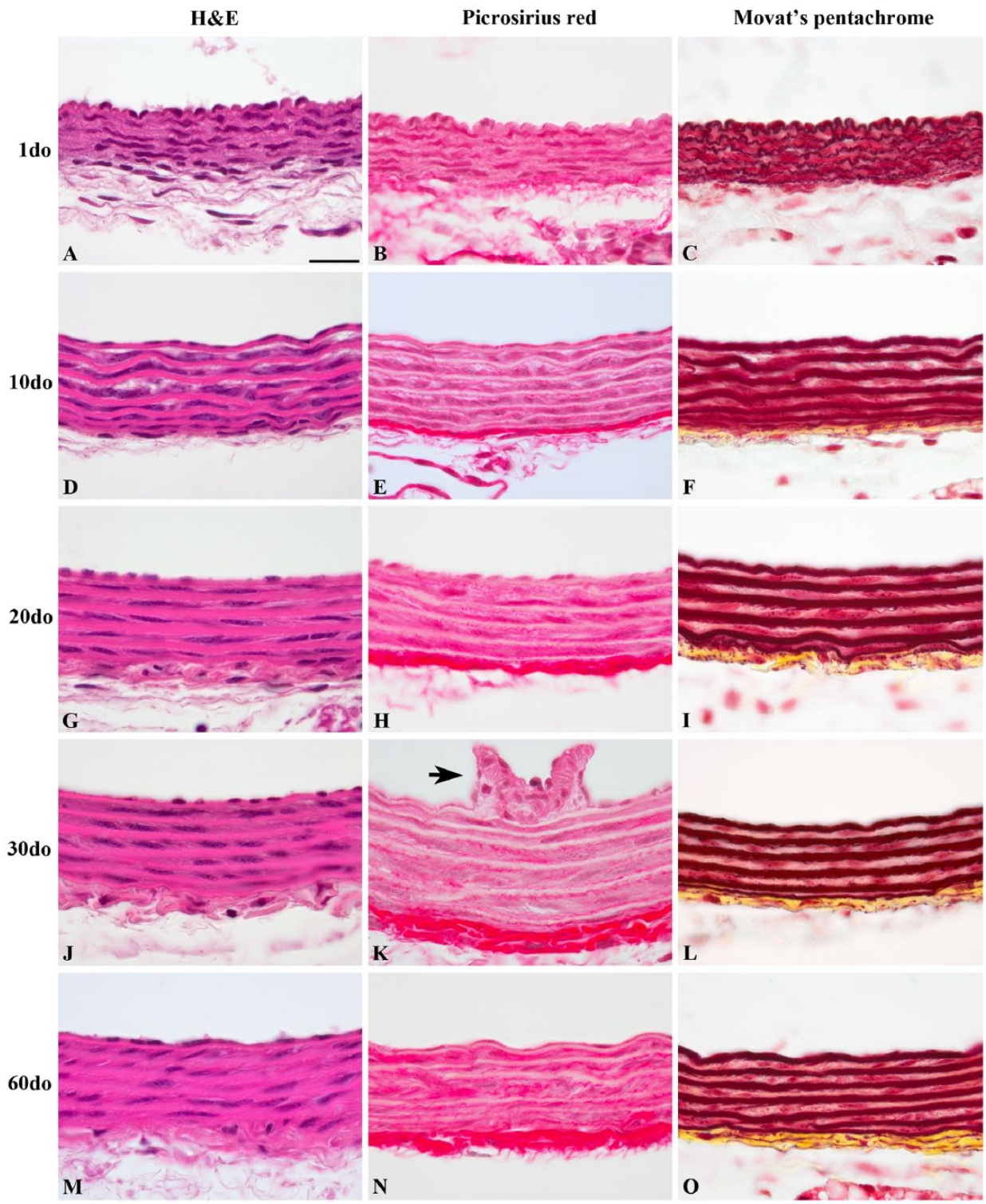

Figure 6. Histological features of representative proximal thoracic aortas (PTAs) from SR-BI$^{-/-}$/ApoeR61$^{h/h}$ mice aged 1–60 days old (do). PTAs were stained with picrosirius red (B, E, H, K, and N) for collagen (red fibrils), and Movat's pentachrome (C, F, I, L and O) for collagen (yellow), elastin (black/red), and glycosaminoglycans (green/blue), for which minimal staining is appreciated. Note the frequent undulation present at 1do (A–C), which dissipates by 10do and is absent in mice aged 20do and older. An intercostal ostium (K, black arrow) with collagenous ridges protruding into the luminal surface can be appreciated within the TA. All images are oriented with luminal surfaces at the top and external adventitial surfaces at the bottom of the photomicrographs. Scale, 20 μm.

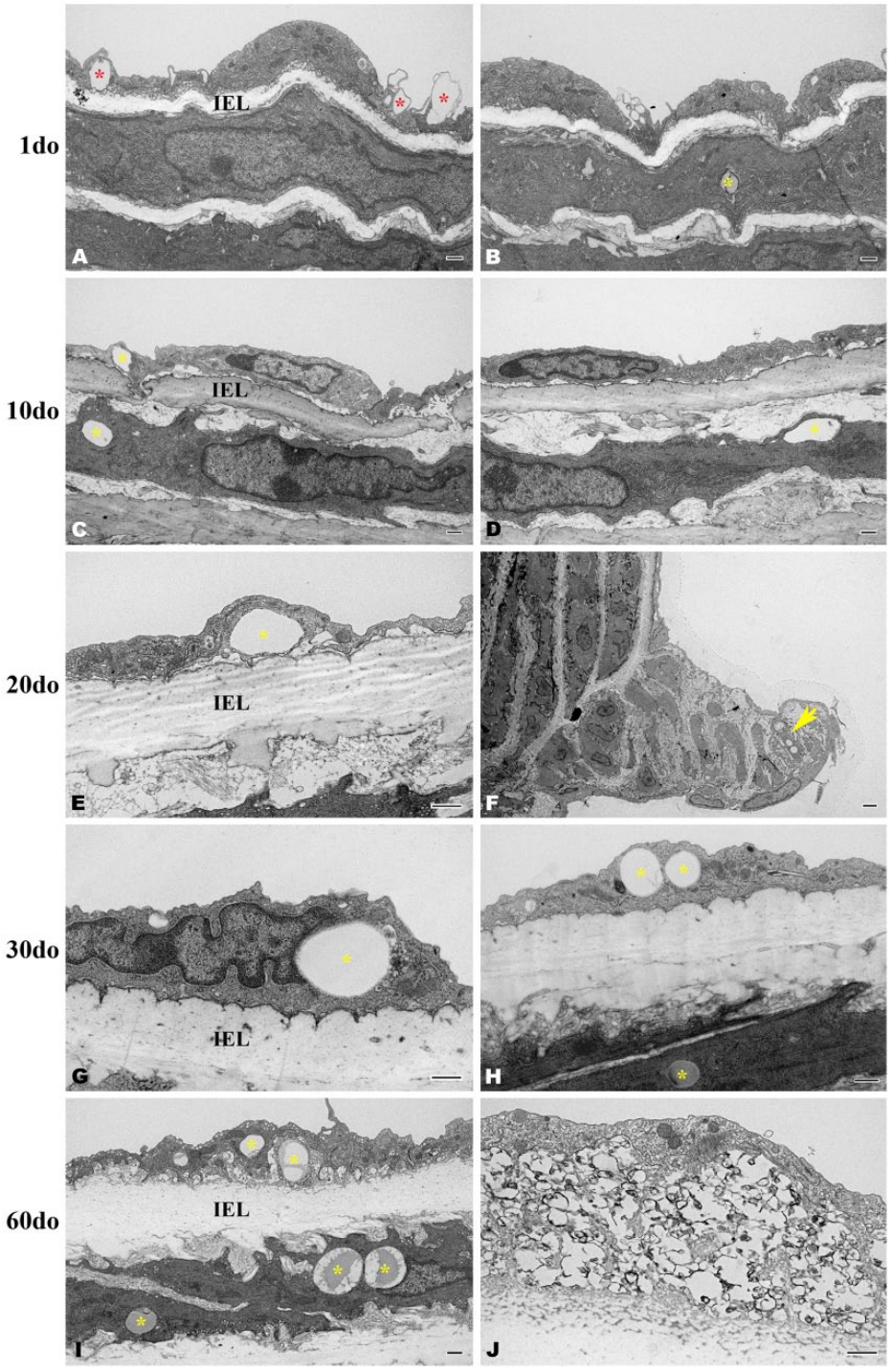

Figure 7. Transverse, osmicated electron micrographs showing the deposition of lipid within the distal thoracic aortic wall of SR-BI$^{-/-}$/ApoeR61$^{h/h}$ mice aged 1-60 days old (do). Variably sized, intracellular lipid can be observed within endothelial cells (C, E, G-I) and within smooth muscle cells (B, C, H-I) directly beneath the internal elastic lamina (IEL) across all age groups, (yellow asterisks). At 1do, lipid is being engulfed by endothelial cells (A, red asterisks). Within an intercostal ostial ridge, lipid droplets are pictured accumulating within a smooth muscle cell (F, yellow arrow). At 60do, an accumulation of intraendothelial, clustered and variably sized lipid droplets admixed with calcified/mineralized debris (black amorphous material) is indicative of early atherosclerotic lesion formation (J). Scale, 500 nm (A–E and G–J) and 2 μm (F).

morphologically consistent with early lipid accumulation by ultrastructure, semi-thin sections stained with Toluidine blue for lipid identification were negative throughout all age groups (histology not shown).

Discussion

Multiphoton imaging has been widely utilized as a powerful tool in studying the macromolecular microstructure of the extracellular matrix in vascular beds. The use of in situ multiphoton microscopy has many benefits including the elimination of tissue fixation as well as extensive exogenous labeling, and it intrinsically permits generation of isotropic 3D images with image registration. Multiphoton microscopy also permits analysis of the tissue in a near physiological setting, minimizing, but not eliminating, residual strain responses, and the fundamental image is performed with en-face planes providing a unique sectioning presentation. Previous studies have shown that the use of multiphoton microscopy contributes to the reduction of artifacts that can sometimes occur with other imaging modalities (So and Kim 1998; So 2002), including reduced photobleaching and phototoxicity.

Here, we have provided a novel, reproducible, in situ dissection of the mouse VTA that, when coupled with this imaging modality, provides valuable insight in healthy arterial morphology indicative of biochemical extracellular matrix status that can further be applied to diseased arteries. Utilization of this preparation decreases potential distortions by minimizing both dissection and mounting artifacts while closely mimicking several key physiological properties. There have been many different approaches used in preparing vessels for ex vivo microscopy reported in the literature. Some have included mounting variably sized vessel segments into a perfusion chamber (Megens et al. 2007a; Megens et al. 2007b), fresh and/or formalin-fixed tissue preparations mounted between a glass slide and a coverslip (Kwon et al. 2008; Lee et al. 2009; Kim et al. 2010, Lim et al. 2010, Lim et al. 2011; Suhalim et al. 2012), as well as agar gel-infused vascular casts that are segmented into thinly sliced molds and mounted on a glass slide (van Zandvoort et al. 2004; Megens et al. 2007a; Megens et al. 2008; Le et al. 2010). In vivo approaches have also been described but these are with the addition of mechanical techniques to help minimize motion artifact. Mouse carotid arteries have been imaged in vivo while mounted on an external apparatus for stabilization during anesthesia (Yu et al. 2007). Both mouse carotid arteries and rat renal arteries have also been imaged using TPEF microscopy triggered on cardiac and respiratory signals (Megens et al. 2010) to reduce motion artifact. Although all preparations provide useful information, fewer perturbations to the vascular bed during dissection, together with maintenance of physiological-like longitudinal stretch and positioning that mimics that observed in vivo, all enhance the in situ relationships of vascular wall matrices. The advantages of this preparation were demonstrated in a cohort of mice aged 1–60do. Findings revealed vessel wall changes associated with a gradual increase in post-natal blood pressure, as previously described (Huang et al. 2005; Le et al. 2012). The undulation within the vessel wall in mice aged 1do and, to a lesser extent, 20do observed using multiphoton microscopy, EM and histopathology, was essentially diminished by 30do, correlating with a rise in blood pressure from approximately 30–70 mmHg from post-natal days 2–35 (Le et al. 2012). These data suggest that, even in the absence of arterial pressure, as imaged in this study, that the remodeling or packing of the individual elastic lamellar units with age was persistent and that the elastic lamellar interconnections with the more rigid collagen fiber bundles increased in mice >30do resulting in tighter packing and less residual strain.

To confirm both the sensitivity and specificity of this preparation for in situ imaging in this longitudinal study, EM and histopathology of the thoracic aortic vascular extracellular matrix were used to validate in situ findings. Both EM and histopathology yielded similar results to multiphoton microscopy regarding the vascular elastic lamellae. Five to six coaxially arranged elastic lamellar layers can be appreciated, with the innermost and outermost layers corresponding to the IEL and EEL, respectively, consistent with results found within the literature (Wolinsky and Glagov 1967; Lee et al. 2005). Collagen fibrils throughout the entire thickness of the vessel wall are best appreciated with multiphoton microscopy, and readily discerned with EM; however, application of picrosirius red for histopathology appeared to be a less sensitive method for the identification of individual collagen fibrils within the tunica media, especially in younger animals. Similarly, Movat's pentachrome showed limited positive collagen staining within the tunica media, but readily elucidated individual elastic lamellar layers. Lipid deposition within the subendothelium and the tunica media was confirmed with EM, but histopathology failed to reveal any lipid deposition at all using well-established techniques, namely, Oil-Red-O and semi-thin frozen sections. Collectively, our data suggests that the multiphoton methodology provided an accurate distribution and structure of the macromolecules in this tissue without fixation or exogenous stains.

An additional benefit from histopathology appreciated in this study was the ability to complete IHC for decorin and biglycan, two members of the SLRP PG family. Both PGs are associated with normal vascular development and vasculopathies, including atherosclerosis, in transgenic mouse models (Williams 2001; Adhikari et al. 2011; Marzoll et al. 2011; Neufeld et al. 2014). The abundance of both PGs observed in this study within the aortic tunica adventitia and, to a lesser extent, the subendothelium and tunica

media, is consistent with previous work completed in murine models (McLean et al. 2005; Adhikari et al. 2011). Furthermore, in IHC sections in which the intercostal ostia were captured (Supplemental Fig. 2C and 2G–2J), strong positive immunoreactivity for both PGs was present within the subendothelium. Given that atherosclerotic lesions in mice often occur at the intercostal ostial bifurcations along the thoracic aorta (McGillicuddy et al. 2001), it is likely that the increased ostial PG deposition observed here in SR-BI KO/ApoeR61$^{h/h}$ mice fed NC will contribute to early lesion development in future atherogenic studies.

Despite the utility of EM and histopathology described here, both imaging modalities have certain limitations in a study such as this. In general, histopathology yields a single, typically 5-µm-thick, two-dimensional (2D) slice from tissue embedded in a paraffin block that can take several days to process. Unless numerous serial sections are produced at deeper steps of the submitted sample, the probability of capturing lipid in a similar study would logically be greatly reduced; in this case, throughout all mice aged 1-60do, we did not detect lipid using limited tissue sections stained with Oil-Red-O. EM, an additional 2D imaging modality, yields higher resolution images with greater resolving power than histopathological sections but also requires time-consuming preparation and production of results from approximately 1 mm×1 mm submitted tissue samples. Similar to limited sampling in histopathology, EM may reduce the likelihood of lipid identification compared to the methods employed in this study. With the in situ aortic preparation developed here, there is no limitation of scanning a small, embedded section. For example, even though the proximal VTA was the defined region of interest, the entire surface of the VTA could be scanned and easily registered into a 3D image without having to resample the original tissue at a later time, as was accomplished in our preliminary studies (Fig. 2).

In summary, this study characterized the developmental changes observed within the ventral (anterior) surface of the proximal thoracic aorta in SR-BI KO/ApoeR61$^{h/h}$ mice maintained under normal dietary conditions utilizing an in situ preparation for multiphoton microscopy. The physical and structural properties were described and further confirmed, albeit with less sensitivity and specificity, using histopathology and EM. Given the physiological similarities with our model to that observed in vivo, we propose that our approach will provide valuable insight into both healthy and diseased arteries in certain pathological conditions, including aortic atherosclerosis, dissections and aneurysms. Future studies involve the investigation, and potential therapeutic intervention, of early atherosclerotic lesion development in SR-BI KO/ApoeR61$^{h/h}$ mice within the proximal thoracic aorta utilizing the present knowledge gained as a reference that defines normal growth within the aortic vascular bed.

Acknowledgments

We thank Alan T. Remaley for providing the original transgenic mouse model breeding pairs, Boris L. Vaismen for providing knowledge regarding the maintenance of SR-BI KO/ApoeR61$^{h/h}$ transgenic mice, and Dahae H. Bae for help preparing sections for electron microscopy. This research was completed in partial fulfillment of dissertation work towards a PhD in Comparative Biomedical Sciences at North Carolina State University College of Veterinary Medicine and the NHLBI, through the NIH Graduate Partnership Program.

Supplementary Material

Supplementary material for this article is available on the *Journal of Histochemistry & Cytochemistry* Web site at http://jhc.sagepub.com/supplemental.

Declaration of Conflicting Interests

The authors declared no potential conflicts of interest with respect to the research, authorship, and/or publication of this article.

Funding

The authors disclosed receipt of the following financial support for the research, authorship, and/or publication of this article: This research was gratefully supported by the intramural research funds of the NIH and the NHLBI as well as the NIH Comparative Biomedical Scientist Training Program.

References

Adhikari N, Carlson M, Lerman B, Hall JL (2011). Changes in expression of proteoglycan core proteins and heparan sulfate enzymes in the developing and adult murine aorta. J Cardiovasc Trans Res 4:313-320.

Dao L, Lucotte B, Glancy B, Chang L-C, Hsu L-Y, Balaban RS (2014). Use of independent component analysis to improve signal-to-noise ratio in multi-probe fluorescence microscopy. J Microsc 256(2):133-144.

de Grauw CJ, Vroom JM, van der Voort HT, Gerritsen HC (1999). Imaging properties in two-photon excitation microscopy and effects of refractive-index mismatch in thick specimens. Appl Opt 38:5995-6003.

Denk W, Stricler JH, Webb WW (1990). Two-photon laser scanning fluorescence microscopy. Science 248:73-76.

Haidari M, Ali M, Gangehei L, Chen M, Zhang W, Cybulsky MI. (2010). Increased oxidative stress in atherosclerosis-predisposed regions of the mouse aorta. Life Sci 87: 100-110.

Huang Y, Guo X, Kassab GS (2005). Axial nonuniformity of geometric and mechanical properties of mouse aorta is increased during postnatal growth. Am J Physiol-Heart C 290:H657-H664.

Kelleher CM, McLean SE, Mecham RP (2004). Vascular extracellular matrix and aortic development. Curr Top Dev Biol 62:153-188.

Kim S-H, Lee E-S, Lee JY, Lee ES, Lee B-S, Park JE, Moon DW (2010). Multiplex coherent anti-stokes raman spectroscopy imaged intact atheromatous lesions and concomitantly

identifies distinct chemical profiles of atherosclerotic lipids. Circ Res 106:1332-1341.

Kwon GP, Schroeder JL, Amar MJ, Remaley AT, Balaban RS (2008). Contribution of macromolecular structure to the retention of low-density lipoprotein at arterial branch points. Circulation 117:2919-2927.

Le TT, Duren HM, Slipchenko MN, Hu C-D, Cheng J-X (2010). Label-free quantitative analysis of lipid metabolism in livin Caenorhabditis elegans. J Lipid Res 51:572-677.

Le VP, Kovacs A, Wagenseil JE (2012). Measuring left ventricular pressure in late embryonic and neonatal mice. J Vis Exp 60:1-7.

Lee JY, Kim S-H, Moon DW, Lee ES (2009). Three-color multiplex CARS for fast imaging and microspectroscopy in the entire CH stretching vibrational region. Opt Express 17:22281-22295.

Lee K, Forudi F, Saidel GM, Penn MS (2005). Alterations in internal elastic lamina permeability as a function of age and anatomical site precede lesion development in apolipoprotein E-null mice. Circ Res 97:450-456.

Lim RS, Kratzer A, Barry NP, Miyazaki-Anzai S, Miyazaki M, Mantulin WW, Levi M, Potma EO, Tromberg BJ (2010). Multimodal CARS microscopy determination of the impact of diet on macrophage infiltration and lipid accumulation on plaque formation in apoE-deficient mice. J Lipid Res 51:1729-1737.

Lim RS, Suhalim JL, Miyazaki-Anzai S, Miyazaki M, Leci M, Potma EO, Tromberg NJ (2011). Identification of cholesterol crystals in plaques of atherosclerotic mice using hyperspectral CARS imaging. J Lipid Res 52:2177-2186

Marzoll A, Melchior-Becker A, Cipollone F, Fischer JW (2011). Small leucine-rich proteoglycans in atherosclerotic lesions: novel targets of chronic statin treatment? J Cell Mol Med 15:232-243.

McLean AE, Mecham BH, Kelleher CM, Mariani TJ, Mecham RP (2005). Extracellular matrix gene expression in the developing mouse aorta. Adv Dev Biol 15:81-128.

McGillicuddy CJ, Carrier MJ, Weinberg PD (2001). Distribution of lipid deposits around aortic branches of mice lacking LDL receptors and apolipoprotein E. Arterioscler Thromb Vasc Biol 21:1220-1225.

Megens RTA, oude Egbrink MGA, Cleutjens JPM, Kuijpers MJE, Schiffers PHM, Merkx M, Slaaf DW, van Zandvoort MAMJ (2007a). Imaging collagen in intact viable healthy and atherosclerotic arteries using fluorescently labeled CNA35 and two-photon laser scanning microscopy. Mol Imaging 6:247-260.

Megens RTA, oude Egbrink MGA, Merkx M, Slaaf DW, van Zandvoort MAMJ (2008). Two-photon microscopy on vital carotid arteries: imaging the relationship between collagen and inflammatory cells in atherosclerotic plaques. J Biomed Opt 13:044022-1 – 044022-10.

Megens RTA, oude Egbrink MGA, Engels W, Leenders PJA, Brunenberg EJL, Reesink KD, Janssen BJA, Romney BMtH (2010). In vivo high-resolution structural imaging of large arteries in small rodents using two-photon laser scanning microscopy. J Biomed Opt 15:011108.

Megens RTA, Reitsma S, Schiffers PHM, Hilgers RHP, DeMey JGR, Slaaf DW, oude Egbrink MGA, van Zandvoort MAMJ (2007b). Two-photon microscopy of vital murine elastic and muscular arteries. J Vasc Res 44:87-98.

Neufeld EB, Zadrozny LM, Phillips D, Aponte A, Yu Z-X, Balaban RS (2014). Decorin and biglycan retain ldl in disease-prone valvular and aortic subendothelial intimal matrix. Atherosclerosis 233:113-121.

Richards-Kortum R, Sevick-Muraca E (1996). Quantitative optical spectroscopy for tissue diagnosis. Ann Rev Phys Chem 47:555-606.

So PTC (2002). Two-photon fluorescence light microscopy. eLS. Macmillan Publishers Ltd, Nature Publishing Group. www.els.net.

So PTC, Kim H (1998). Two-photon deep tissue ex vivo imaging of mouse dermal and subcutaneous structures. Opt Express 3:339-350.

Strupler M, Pena AM, Hernest M (2007). Second harmonic imaging and scoring of collagen in fibrotic tissues. Opt Express 15:4054-4065.

Suhalim JL, Chung C-Y, Lilledahl MB, Lim RS, Leci M, Tromberg BJ, Potma EO (2012). Characterization of cholesterol crystals in atherosclerotic plaques using stimulated raman scattering and second-harmonic generation microscopy. Biophys J 102:1988-1995.

Supatto W, Debarre D, Moulia B, Brouzes E, Martin JL, Farge E, Beaurepaire E (2005). In vivo modulation of morphogenetic movements in Drosphilia embryos with femtosecond laser pulses. Proc Natl Acad Sci U S A 102:1047-1052.

Tangirala RK, Rubin EM, Palinski W (1995). Quantitation of atherosclerosis in murine models: correlation between lesions in the aortic origin and in the entire aorta, and differences in the extent of lesions between sexes in LDL receptor-deficient and apolipoprotein E-deficient mice. J Lipid Res 36:2320-2328.

Van Zandvoort M, Engels W, Douma K, Beckers L, oude Egbrink M, Daemon M, Slaaf DW (2004). Two-photon microscopy for imaging of the (atherosclerotic) vascular wall: A proof of concept study. J Vasc Res 41:54-63.

Wagenseil JE, Mecham RP (2009). Vascular extracellular matrix and arterial mechanics. Phusiol Rev 89:957-989.

Williams KJ (2001). Arterial wall chondroitin sulfate proteoglycans: diverse molecules with distinct roles in lipoprotein retention and atherogenesis. Curr Opin Lipidol 12:477-487.

Wolinsky H, Glagov S (1967). A lamellar unit of aortic medial structure and function in mammals. Circ Res 20:99-111.

Yu W, Braz JC, Dutton AM, Prusakov P, Rekhter M (2007). In vivo imaging of atherosclerotic plaques in apolipoprotein E deficient mice using nonlinear microscopy. J Biomed Opt 12:054008

Yue S, Slipchenko MN, Cheng J (2011). Multimodal nonlinear optical microscopy. Laser Photonics Rev 5:496-512.

Zhang S, Picard M, Vasile E, Zhu Y, Raffai R, Weisgraber K, Krieger M (2005). Diet-induced occlusive coronary atherosclerosis, myocardial infarction, cardiac dysfunction, and premature death in scavenger receptor class B Type I-deficient, hypomorphic apolipoprotein ER61 mice. Circulation.111:3457-3464.

Zipfel WR, Williams RM, Christie R, Nikitin AY, Hyman BT, Webb WW (2003). Live tissue intrinsic emission microscopy using multiphoton-excited native fluorescence and second harmonic generation. Proc Natl Acad Sci U S A 100: 7075-7080.